photonics

MDPI

Article

Detection of CO_2 and CH_4 Concentrations on a Beijing Urban Road Using Vehicle-Mounted Tunable Diode Laser Absorption Spectroscopy

Jiuying Chen [1], Pengxiang Cui [1,2], Chuncheng Zhou [1], Xiaoya Yu [3], Haohao Wu [1], Liangquan Jia [4,*], Mei Zhou [1,*], Huijing Zhang [1], Geer Teng [1], Sai Cheng [1], Linsheng Chen [1] and Yuanyuan Qiu [1]

1 Key Laboratory of Quantitative Remote Sensing Information Technology, Aerospace Information Research Institute, Chinese Academy of Sciences, Beijing 100094, China; chenjy@aircas.ac.cn (J.C.)
2 School of Electronic, Electrical and Communication Engineering, University of Chinese Academy of Sciences, Beijing 100049, China
3 Key Laboratory of Experimental Physics and Computational Mathematics, Beijing 100094, China
4 School of Information Engineering, Huzhou University, Huzhou 313000, China
* Correspondence: 02426@zjhu.edu.cn (L.J.); zhoumei@aoe.ac.cn (M.Z.)

Abstract: The analysis of greenhouse gas emission characteristics on urban roads is of great significance for understanding the sources and sinks of urban greenhouse gases and their changing patterns. Based on tunable diode laser derivative absorption spectroscopy technology, which features high resolution, high sensitivity, and fast response, a vehicle-mounted system capable of simultaneously detecting CO_2 and CH_4 has been developed. The system has a response time of 0.38 s, with detection sensitivities of 5 ppb for CH_4 and 0.2 ppm for CO_2, power consumption of approximately 4.8 W, a weight of less than 3 kg, and dimensions of 255 mm × 275 mm × 85 mm. Using this system, monitoring campaigns were conducted on the same road in Beijing, running north–south, during different time periods in April and June 2023. The results show that there is little correlation between changes in CO_2 and CH_4 concentrations on the road, and these gas concentrations exhibit different influencing factors and spatiotemporal characteristics. The CO_2 concentration on the road is primarily related to the degree of traffic congestion and does not exhibit significant seasonal variations. The average CO_2 concentration measured on the road is much higher than the global average CO_2 concentration during the same period. On the other hand, the CH_4 concentration on the road is not strongly correlated with traffic congestion but is closely related to the leakage of methane from specific emission wells or covers. The CH_4 concentration is higher in the morning, gradually decreases as the sun rises, and then increases again after sunset. The CH_4 concentration measured at night in June is significantly lower than that in April, reflecting some seasonal variation. The CH_4 concentration on the Beijing urban road is slightly higher than the global average CH_4 concentration during the same period. The vehicle-mounted experiments verified the feasibility of using this self-developed system for vehicle-mounted detection of greenhouse gas concentrations on urban roads. The research results can provide data for analyzing the spatial pattern of regional carbon sources and sinks.

Keywords: tunable diode laser absorption spectroscopy (TDLAS); derivative absorption spectroscopy; CO_2; CH_4

Citation: Chen, J.; Cui, P.; Zhou, C.; Yu, X.; Wu, H.; Jia, L.; Zhou, M.; Zhang, H.; Teng, G.; Cheng, S.; et al. Detection of CO_2 and CH_4 Concentrations on a Beijing Urban Road Using Vehicle-Mounted Tunable Diode Laser Absorption Spectroscopy. *Photonics* **2023**, *10*, 938. https://doi.org/10.3390/photonics10080938

Received: 20 July 2023
Revised: 14 August 2023
Accepted: 14 August 2023
Published: 17 August 2023

1. Introduction

Greenhouse gases in the atmosphere mainly include carbon dioxide (CO_2), methane (CH_4), perfluorocarbons (PFCS), hydrofluorocarbons (HFCS), nitrous oxide (N_2O), and others. These gases absorb the outgoing longwave radiation emitted by the Earth's surface, leading to the greenhouse effect in the Earth's atmosphere [1]. The greenhouse effect results in a range of environmental and economic issues and has a significant impact on the human living environment and quality of life [1,2]. Achieving high-precision detection

of greenhouse gases and accurately monitoring their concentrations and variations in the ambient atmosphere is of great importance as it provides valuable insights used for predicting future climate change [3]. According to data released by NOAA [4], the global average CO_2 concentration in April 2023 was 420.54 ppm, an increase of 2.12 ppm compared to April 2022. The global average CH_4 concentration in March 2023 was 1920.74 ppb, showing an increase of 11.77 ppb compared to March 2022. The continuous increase in CO_2 and CH_4 concentrations has led to global atmospheric warming and ecological hazards, making them significant environmental concerns [5–7]. With the deepening impact of global changes, achieving the goal of "emission peak and carbon neutrality" has become a consensus in the international community. CO_2 and CH_4, as the most important greenhouse gases, have been the focus of research both domestically and internationally and are key monitoring targets for many countries [8,9]. Therefore, studying the spatial and temporal distribution patterns of CO_2 and CH_4 concentrations in the atmosphere is of great significance for understanding and grasping the global carbon cycle and addressing global climate change.

Urban activities are significant sources of greenhouse gas emissions, with the increasing number of urban buses and freight vehicles, as well as their travel distances, comprising one of the major contributors to the rise in urban greenhouse gas emissions. Therefore, analyzing the emission characteristics of greenhouse gases from urban road surfaces is of crucial importance for understanding the sources and sinks of urban greenhouse gases, as well as the patterns of their variations over time. Currently, long-term observations of greenhouse gases by the meteorological departments in China primarily focus on atmospheric background observation stations such as Waliguan, Shangdianzi, Lin'an, and Longfengshan. These atmospheric background observation stations are located far from urban areas and can reflect regional variations in atmospheric greenhouse gas concentrations, but they cannot provide information on urban emissions. In recent years, scholars have conducted studies on greenhouse gas concentrations in urban road environments. For instance, Xinmu Zhang et al. [10] utilized a vehicle-mounted greenhouse gas observation system (Portable $CO_2/CH_4/H_2O$ Analyzer, model 915-0011, Los Gatos Research, Mountain View, CA, USA) and selected three routes spanning the main urban area of Nanjing to conduct a four-day mobile observation of atmospheric CO_2 and CH_4 concentrations, analyzing the variations in CO_2 and CH_4 concentrations in Nanjing's urban area. Mingdi Zhang et al. [11] employed a Uow FITR greenhouse gas analyzer (ECOTECH Pty. Ltd., Melbourne, Australia) and conducted a nearly year-long continuous observation experiment on greenhouse gas emissions from road traffic sources at roadside monitoring sites in Shenzhen, analyzing the concentration levels, seasonal patterns, and daily variations of greenhouse gases in Shenzhen. Ruonan Li et al. [12] similarly used a portable $CO_2/CH_4/H_2O$ analyzer (model 915-0011) to observe near-surface atmospheric CO_2 and CH_4 concentrations in Hangzhou's road environment during the winter of 2020 and the spring of 2021, analyzing the spatial representativeness and hotspot identification of urban measurement sites. Bu Zhao et al. [13] installed low-cost particulate matter (PM2.5) sensors on 260 electric vehicles in taxi fleets, creating an air pollution map of Beijing. The accuracy of CO_2 and CH_4 measurement retrievals on a 200 m laser path was estimated at 20 ppm (4.8%) and 60 ppb (3.1%), respectively [14]. The detection repeatability of the carbon dioxide detector based on tunable semiconductor laser absorption spectroscopy was 0.4%, and the detection accuracy was 10 mg/m^3 (~5.5 ppm) [15]. The average concentration during the measurement period was 802.6 ppm, with a range of variation between 797 ppm and 807 ppm, with a difference of approximately 10 ppm for CO_2 [16]. The "time division multiplexing" methane and carbon dioxide detection system stability was higher than 95.3%, and the detection error was less than 4.3% [17]. The measurement lower limit for the CH_4 gas absorption spectral line at 1653.73 nm, with a measurement path length of 60 cm, was 13.6 ppm. The measurement lower limit for the CO_2 gas absorption spectral line was 5625 ppm [18].

This study conducted experiments to detect CO_2 and CH_4 gas concentrations on a Beijing urban road using a self-developed prototype of a high-sensitivity CO_2 and CH_4

detection system. The detection system is based on TDLAS (tunable diode laser absorption spectroscopy) derivative absorption spectroscopy technology and employs a simple wave pool with an optical path length of up to 40 m. The sensitivity of the instrument reaches 5 ppb for CH_4 and 0.2 ppm for CO_2, with a power consumption of approximately 4.8 W and a weight of less than 3 kg. In April and June 2023, real-time experiments were conducted on a Beijing urban road to detect the concentrations of CO_2 and CH_4 gases. The average concentrations and variations of CO_2 and CH_4 gases on the test roads of the Beijing urban area were obtained, validating the feasibility of the self-developed system for vehicle-mounted detection of road greenhouse gas concentrations.

2. Principles and Analysis of Measurement

2.1. Basic Principles and Concepts

The basic principle of TDLAS technology is based on the Beer–Lambert law, which states [19]:

$$I_t(\nu) = I_0(\nu)T(\nu) = I_0(\nu)\exp(-k_\nu L) \tag{1}$$

where $I_0(\nu)$ represents the incident light intensity (in mW); $I_t(\nu)$ represents the transmitted light intensity (in mW); ν is the frequency of the incident light (in cm^{-1}); $T(\nu)$ refers to the spectral transmittance (dimensionless); k_ν is the spectral absorption coefficient (in cm^{-1}); and L represents the effective absorption optical path length (in cm).

For a single transition i,

$$k_\nu = Px_{abs}S_i(T)\varphi_\nu \tag{2}$$

where P is the static total pressure of the gas mixture (in atm); x_{abs} represents the volume concentration of the absorbing gas; $S_i(T)$ is the line strength of transition i at temperature T (in $cm^{-2}{\cdot}atm^{-1}$); and φ_ν represents the normalized line shape function, with $\int \varphi_\nu d\nu = 1$.

Based on Equations (1) and (2), the absorbance $A(\nu)$ and integrated absorbance A_i can be obtained as follows:

$$A(\nu) = ln\left(\frac{I_0}{I_t}\right) \tag{3}$$

$$A_i = \int ln\left(\frac{I_0}{I_t}\right)d\nu = Px_{abs}S_i(T)L \tag{4}$$

Based on Equation (4), when the total pressure of the gas mixture, gas absorption optical path length, and temperature are given, the gas volume concentration can be obtained by substituting the integrated absorbance A_i into the aforementioned equation.

2.2. Principle of Derivative Absorption Spectroscopy Technique

When computing integrated absorbance in direct absorption spectroscopy, there is a stringent requirement for accurate baseline fitting, and the integration process is time-consuming and computationally demanding. In contrast, derivative absorption spectroscopy, akin to wavelength modulation spectroscopy (WMS), has emerged as an advancement built upon the foundation of direct absorption spectroscopy. It presents the advantage of mitigating background interference and enhancing the signal-to-noise ratio.

The second derivative of Equation (1) is obtained as follows [20]:

$$I_t'' = T''(\nu)I_0(\nu) + 2T'(\nu)I_0'(\nu) + T(\nu)I_0''(\nu) \tag{5}$$

Due to the adoption of a sawtooth wavelength scanning technique, the laser output ideally exhibits a linear variation with respect to the current, leading to $I_0''(\nu) = 0$. In Equation (5), the third term can be directly omitted (although in practical measurements this term is nonzero due to the nonlinearity between laser output power and current, it is significantly smaller than the first term). The second term is zero at the center position of the absorption peak, and its influence manifests as asymmetry in the waveform of the second derivative.

In the case where pressure broadening dominates, the dominant line shape follows the Lorentzian profile and can be expressed as follows [21]:

$$\phi_L(\nu) = \frac{1}{\pi\Delta\nu_L}\frac{1}{1+[(\nu-\nu_0)/\Delta\nu_L]^2} \tag{6}$$

where $\Delta\nu_L$ (in cm^{-1}) represents the half-width at half-maximum (HWHM) of the Lorentzian line shape, while ν_0 represents the center frequency. Thus, the value of $T''(\nu)$ at the center frequency in the first term of Equation (5) is

$$T''(\nu_0) = -SPxL\phi''(\nu_0)T(\nu_0) \tag{7}$$

By utilizing Equations (1), (2), and (6), the following conclusions can be drawn:

$$\phi(\nu_0) = \frac{1}{\pi\Delta\nu_L} \tag{8}$$

$$T(\nu_0) = \exp\left(-\frac{SPxL}{\pi\Delta\nu_L}\right) \tag{9}$$

$$\phi''(\nu_0) = \frac{-2}{\pi(\Delta\nu_L)^3} \tag{10}$$

Hence:

$$I_t''(\nu_0) = T''(\nu_0)I_0(\nu_0) = SPxL\frac{2}{\pi(\Delta\nu_L)^3}\exp\left(-\frac{SPxL}{\pi\Delta\nu_L}\right)I_0(\nu_0) \tag{11}$$

where, in the case of weak gas absorption, $\exp\left(-\frac{SPxL}{\pi\Delta\nu_L}\right)$ can be approximated as 1, and $I_t''(\nu_0)$ is approximately linearly related to the gas volume concentration (x) [22]. Therefore, by measuring the peak values of the derivative absorption spectra obtained from different concentration standard gases, the relationship between gas concentration and peak value can be established, enabling the determination of gas concentration.

3. Experimental Device and Spectral Processing

The development of a vehicle-mounted detection system based on the tunable diode laser derivative absorption spectroscopy technique has been accomplished. The system architecture, as illustrated in Figure 1, consists of optical and electronic components in the hardware section, while the software section encompasses the system workflow and spectral data processing.

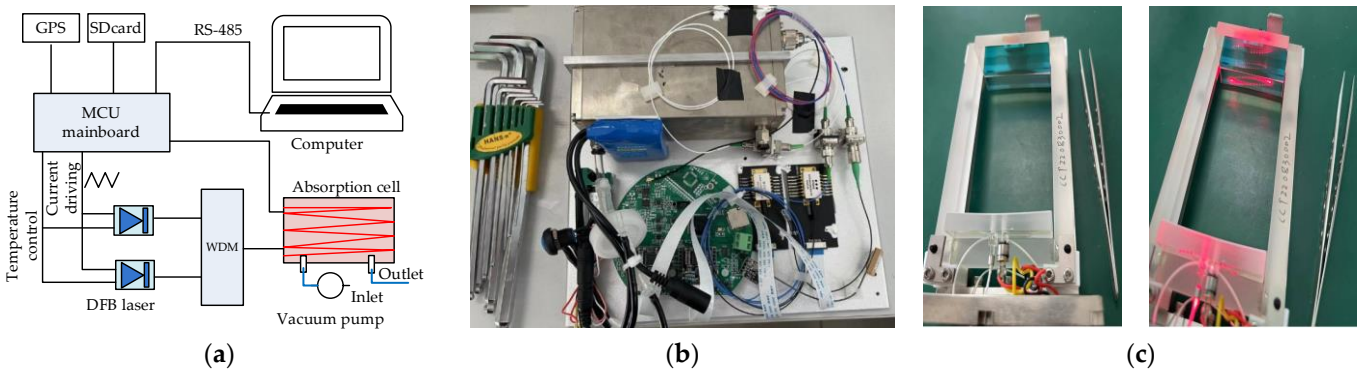

Figure 1. Schematic diagram of experimental device (**a**), system physical photo (**b**), and multipass cell geometry (**c**).

3.1. Hardware Section

The hardware section consists of the optical and electronic components, with the key component in the optical part being the multipass cell (SPEC-PD-192, Xuhai Opto-Electronic Technologies Co., Ltd., Xuzhou, China) [23], which is shown in Figure 1c. The multipass cell is designed for fiber-optic input and detector output, with a single optical path length of 12.9 cm and 310 passes, achieving an absorption path length of approximately 40 m. The outgoing light is directly received by the detector installed at the emission port of the gas cell, completing the photoelectric signal conversion. The WDM (wavelength division multiplexing) combines two laser beams and feeds them into the multipass cell.

The electronic component comprises several modules including the laser temperature control and current driver module, sawtooth signal generation module, detector current-to-voltage conversion module, automatic gain module, AD conversion and concentration calculation storage module, and GPS signal acquisition module. The chosen microcontroller unit (MCU) is the STM32H743 processor with an ARM Cortex-M7 core, operating at a high frequency of up to 400 MHz. It possesses abundant peripherals and features, enabling efficient execution of floating-point operations for derivative spectrum and concentration calculations. Time, latitude, longitude, altitude, and concentration results are stored on a microSD card and can be uploaded to a host computer via RS-485 communication. The system can be powered by a lithium battery or an external power supply, consuming approximately 4.8 W. Its total weight is less than 3 kg, and the dimensions are 255 mm × 275 mm × 85 mm.

The detection of CH_4 utilizes a distributed feedback (DFB) laser with a center wavelength of 1653.72 nm (W1653B-12-A, W Chip TECH LTD, Xinzhu, China), while the detection of CO_2 employs a DFB laser with a center wavelength of 2005.09 nm (EP2004-DM-B, eblanaPhotonics, Dublin, Ireland). By controlling the current injection and ensuring the stability of the lasers' operation, the wavelength scanning range of the lasers encompasses a complete absorption line of the target gas. The scanning repetition frequency is set at 1 kHz, and the update rate for concentration data is one value every 0.38 s.

3.2. Software Section

The software section is primarily managed by the MCU as the central control chip. The MCU not only coordinates the operation of peripheral modules but also handles data acquisition and spectral processing for gas concentration calculations. The software flow of the system is illustrated in Figure 2. The software functionality encompasses system initialization and parameter configuration, data acquisition, data processing, hardware control, data transmission, and storage capabilities. Upon software startup, the system undergoes initialization. A dedicated file is used for loading and storing parameters, ensuring automatic parameter retrieval during program execution. During initialization, the parameters from the previous run are read from the parameter file. If the read is successful, all parameters are set to their respective values from the last execution. In case of failure to read (the first run after installation), default system parameter values are used for configuration. Subsequently, the system can operate continuously. Data acquisition includes GPS signals, temperature, and spectral data collection. The spectral data acquisition is configured based on specific requirements, including sampling length, accumulation average count, and other parameters. It captures raw data containing absorption information for CO_2 and CH_4. Data processing primarily involves cumulative averaging, digital filtering, derivative spectrum calculation, peak detection, and wavelength locking on the raw data. Ultimately, gas concentrations are computed, and real-time data such as time, temperature, latitude, longitude, altitude, and CH_4 and CO_2 concentrations are stored in the SD card. Simultaneously, these data are transmitted to a host computer via RS-485 communication. Hardware system control includes reading system parameters, which are stored in the external EEPROM. During system power-up, parameters such as the central wavelength of the light source, baud rate, and GPS time are automatically retrieved. Writing system

parameters primarily involves setting the laser's central wavelength, temperature, and baud rate using the RS-485 protocol.

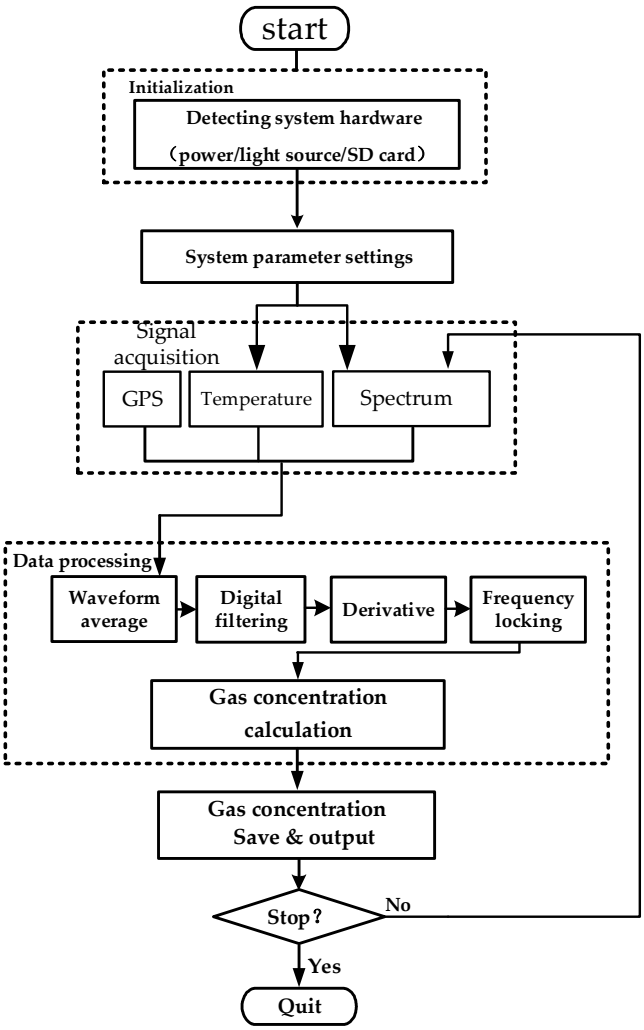

Figure 2. Flowchart of software operation.

4. Results and Discussion

4.1. System Calibration

The vehicle-mounted TDLAS system primarily detects the concentrations of CH_4 and CO_2 in the atmosphere. The CH_4 concentration in the atmosphere is approximately 2 ppm, while the CO_2 concentration is around 400 ppm. In indoor environments, such as crowded rooms, the CO_2 concentration can reach up to 800 ppm. Therefore, during system calibration, standard gases with concentrations close to those found in the atmosphere are used. The following example focuses on the calibration process for CH_4.

The calibration experiments were conducted using high-purity nitrogen gas and standard gas mixtures with CH_4 concentrations of 1.3 ppm, 2.6 ppm, 3.3 ppm, and 5.4 ppm, respectively. During the experiment, the standard gases were introduced into the system inlet through a flow meter (flow rate of 2 L/min). Each concentration was measured for a period of more than 20 min, and the derivative spectrum was collected after complete stabilization, as shown in Figure 3.

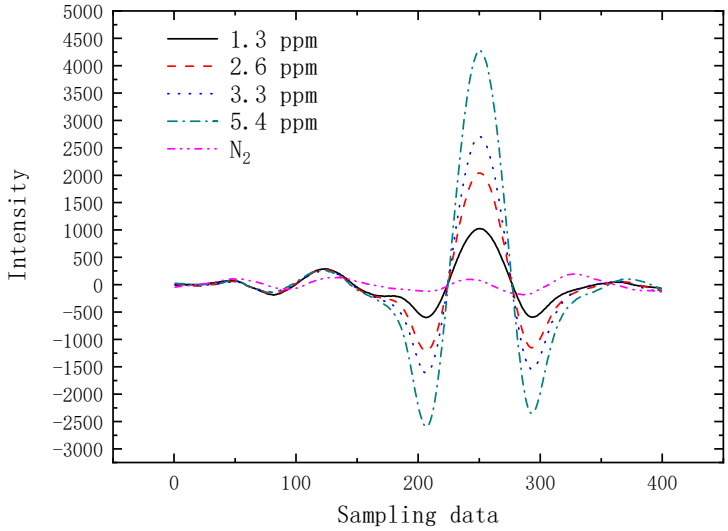

Figure 3. The derivative spectrum of gases with different concentrations.

Two fitting methods were used in this study: the amplitude from the peak to the left valley and the amplitude from the peak to the right valley for fitting. The results are shown in Figure 4. As can be seen from the figure, both methods have good fitting effects, with R^2 values of 0.99831 and 0.99794, respectively. The first method is slightly better than the second method. Therefore, the system uses the fitting parameters obtained from the first method:

$$y = 114.79689 + 1247.36978x$$

where y represents the peak-to-peak value of the derivative spectrum, which is a unitless quantity, and x represents the gas concentration in ppm. During the measurement process, the corresponding gas concentration value is calculated based on the measured y value.

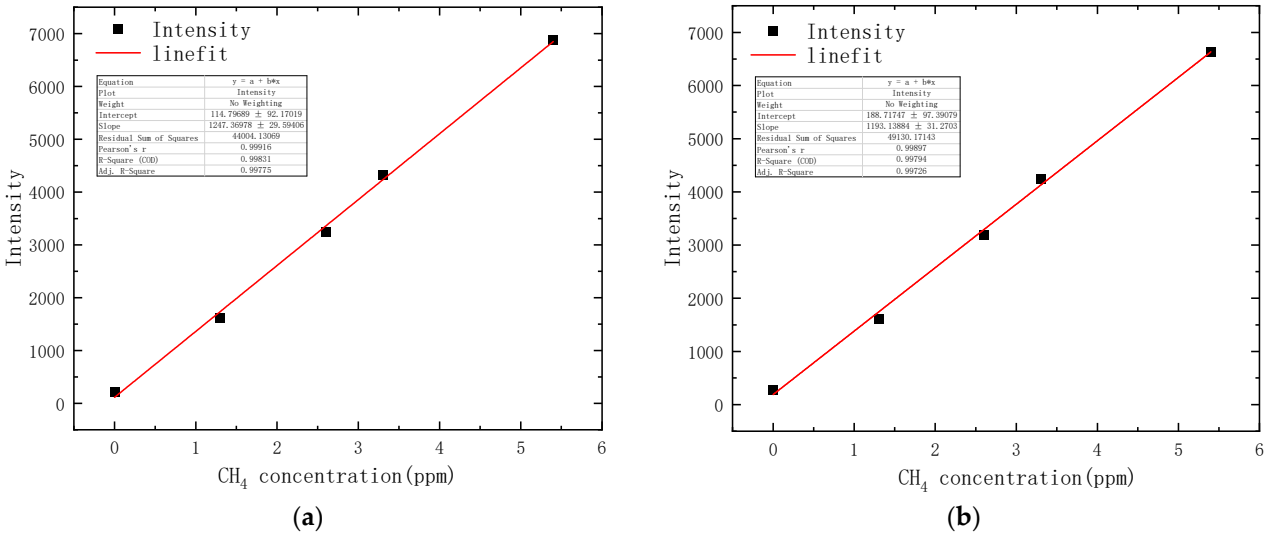

Figure 4. Peak-to-peak values and fitting results of gases with different concentrations: (**a**) using the amplitude from the peak to the left valley; and (**b**) using the amplitude from the peak to the right valley.

4.2. System Performance

Using the system to perform multiple blank tests (such as using zero-gas experiments), the standard deviation of background response is derived. The detection limit of the system is defined as three times the standard deviation (3σ) measured during blank testing [24].

$$3\sigma = 3\sqrt{\frac{\sum_{i=1}^{n}\left(C_i - \overline{C}\right)^2}{n}} \tag{12}$$

The sensitivity of the system is defined as the standard deviation (σ) measured during blank testing [24]. The detection precision is expressed by the standard deviation under certain measurement conditions. The accuracy (A) is indicated by the degree to which the average of multiple measurements under specific experimental conditions aligns with the true value.

$$A = \frac{\frac{1}{n}\sum_{i=1}^{n} C_i - C}{C} \tag{13}$$

In the experiment, high-purity nitrogen gas was used as a blank test to measure the detection limit and sensitivity of the system. The detection accuracy and precision of the system were evaluated using a standard mixture of 1.0 ppm CH_4, 307 ppm CO_2, and N_2. The results of the blank test are shown in Figure 5. Based on the measurement results over a continuous 5 min period, the detection limit of the system was determined to be 15 ppb for CH_4 and 0.5 ppm for CO_2, while the system sensitivity was found to be 5 ppb for CH_4 and 0.2 ppm for CO_2.

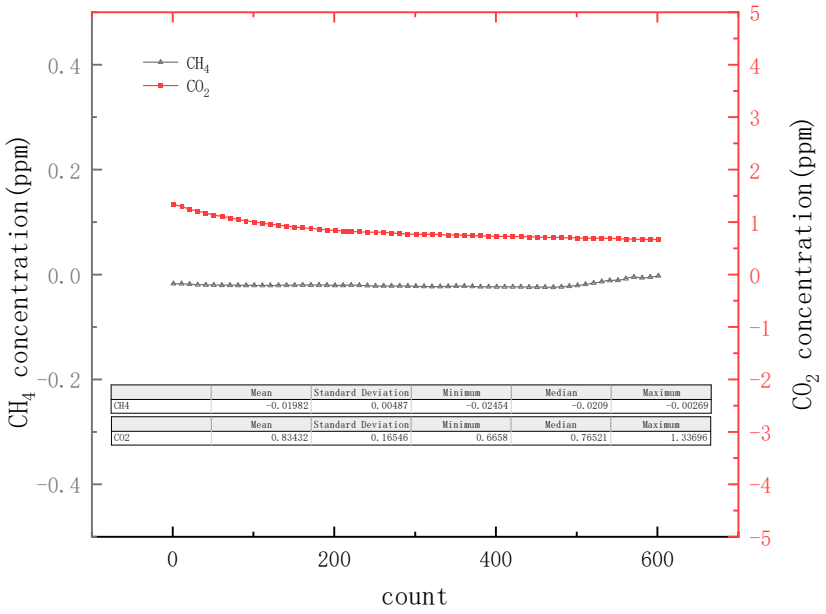

Figure 5. Blank test results.

Using the system to measure a standard mixture of 1.0 ppm CH_4, 307 ppm CO_2, and N_2, the results were obtained as shown in Figure 6. Based on the statistical analysis, the detection precision of the system was determined to be 4 ppb for CH_4 and 37 ppb for CO_2, while the accuracy was 2.3% for CH_4 and 1.6% for CO_2.

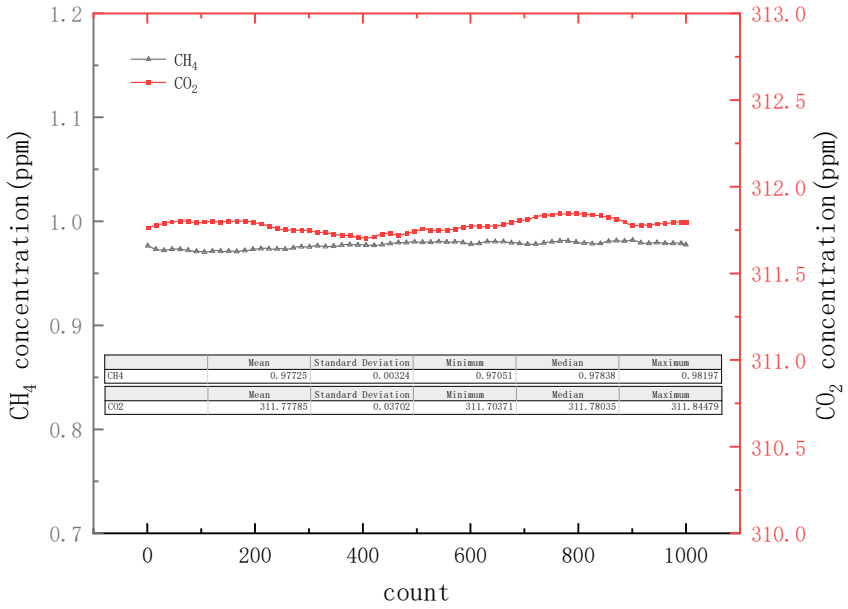

Figure 6. Test results of standard mixture of 1.0 ppm CH_4, 307 ppm CO_2, and N_2.

4.3. Road Measurement Results

The system was used for navigation monitoring along the roads between Dengzhuang South Road (longitude 116.282123° E, latitude 40.070738° N) and Shicao East Road (longitude 116.251248° E, latitude 39.90029° N) in the Beijing urban area. The monitoring was conducted on 24–27 April 2023 and 12–14 June 2023. The travel route spanned north and south, covering a distance of approximately 25 km. The route passed through Dengzhuang South Road–Youyi Road–Dongbeiwang West Road–Malianwa North Road–Yuanmingyuan West Road–Wanquanhe Road–North Fourth Ring West Road–West Fourth Ring North Road–West Fourth Ring Middle Road–Lianshi East Road–Yuquan Road–Shicao East Road, as shown in Figure 7.

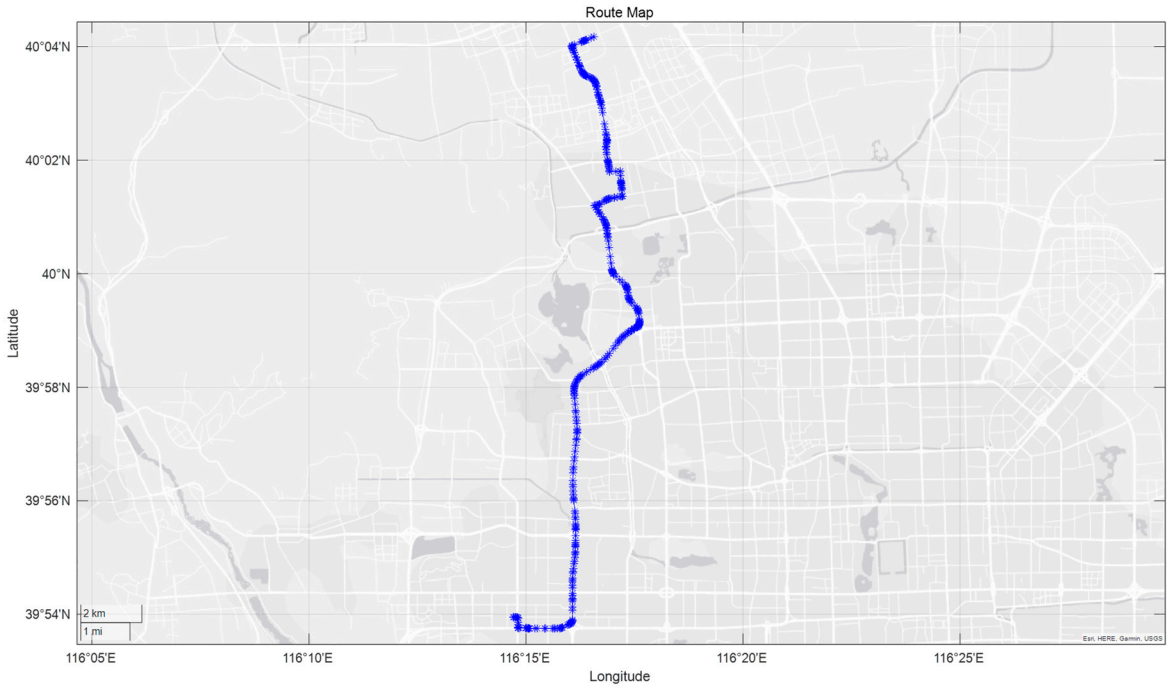

Figure 7. Driving track diagram.

The monitoring experiments were carried out in morning rush hour and three time periods during the nighttime, respectively. The variations in CO_2 and CH_4 concentrations from south to north during the morning rush hour are shown in Figures 8 and 9, respectively. The statistical analysis data are presented in Table 1. From Figure 8, it can be observed that the CO_2 concentration on the road during the morning rush hour is primarily related to traffic congestion. The peaks in the graph correspond to the impact of vehicle exhaust during congested periods, with higher peaks indicating more severe congestion. According to Table 1, there is no significant seasonal variation in CO_2 concentration on the road during the morning rush hour. The average concentrations measured during the same time period over five days ranged from 549 ppm to 587 ppm. The average concentration for three days in April was 549.62 ppm, which is 30.69% higher than the NOAA-published global average CO_2 concentration of 420.54 ppm for April. This difference is primarily due to the monitoring of CO_2 gas concentrations on the road during the morning rush hour in this experiment.

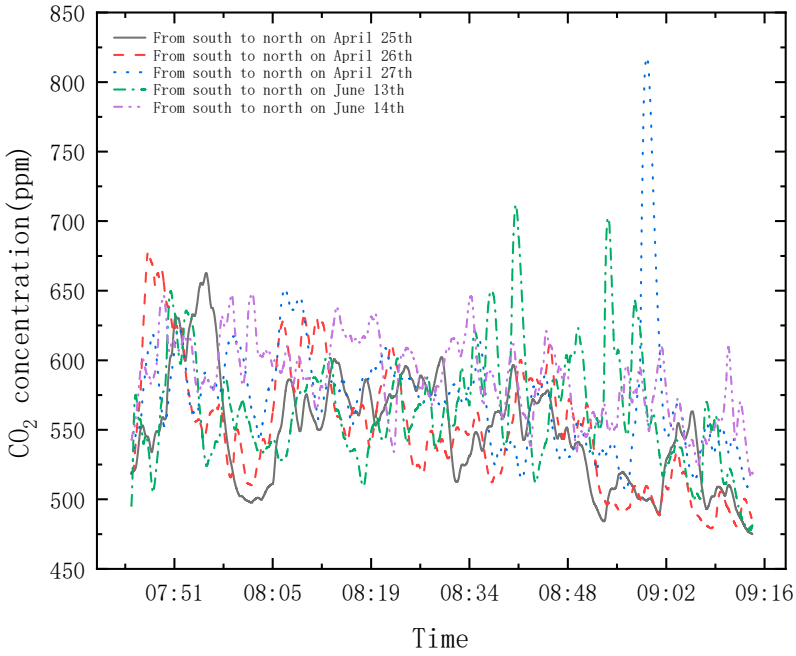

Figure 8. CO_2 concentration measured from south to north on the experimental road section during morning rush hour.

Table 1. Statistical analysis of CO_2 and CH_4 concentrations measured during morning rush hour.

Gas	Date	Period	Mean Value (ppm)	Standard Deviation (ppm)	Minimum Value (ppm)	Median (ppm)	Maximum Value (ppm)
CO_2	25 April 2023	7:55–9:12	549.6	39.6	475.1	550.2	662.7
	26 April 2023	7:56–9:13	551.5	44.9	479.2	549.0	678.0
	27 April 2023	7:59–9:17	573.4	43.9	504.7	572.3	818.5
	13 June 2023	7:45–9:11	564.8	40.8	477.8	558.6	711.5
	14 June 2023	7:45–9:15	587.0	27.9	515.8	587.8	648.2
CH_4	25 April 2023	7:55–9:12	2.124	0.175	1.920	2.032	2.694
	26 April 2023	7:56–9:13	2.167	0.175	1.859	2.188	2.481
	27 April 2023	7:59–9:17	2.144	0.137	1.986	2.092	2.440
	13 June 2023	7:45–9:11	2.168	0.216	1.815	2.099	2.651
	14 June 2023	7:45–9:15	2.085	0.252	1.801	2.049	3.302

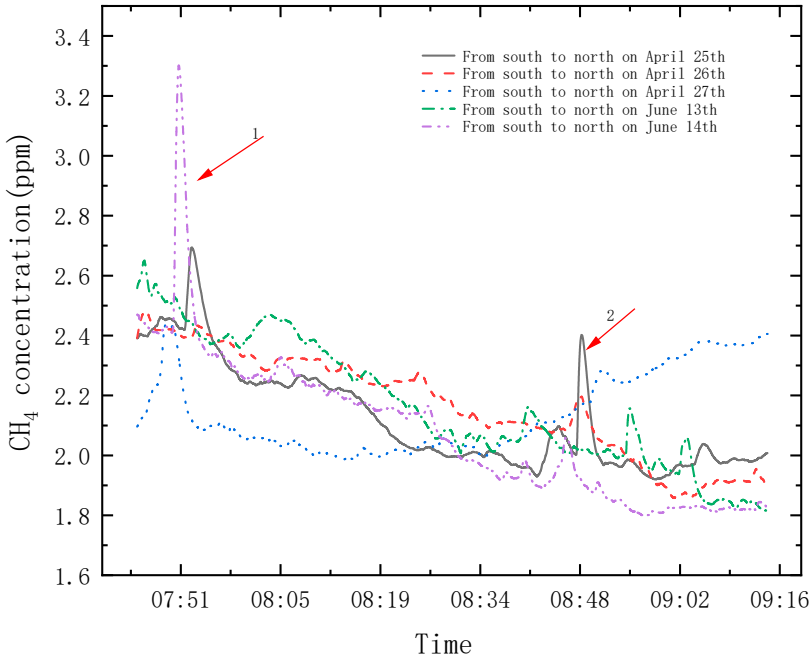

Figure 9. CH_4 concentration measured from south to north on the experimental section during morning rush hour.

Figure 10 illustrates the correlation analysis between CO_2 and CH_4 concentrations measured during the morning rush hour along the experimental route from south to north. The correlation between CO_2 and CH_4 concentrations is only 0.46, indicating a moderate positive correlation. From Figure 9, it can be observed that the CH_4 concentration on the road during the morning rush hour is not significantly correlated with traffic congestion but exhibits a noticeable downward trend. This pattern reflects the diurnal variation in CH_4 concentration, with higher concentrations observed in the early morning that gradually decrease as the sun rises. Further investigation reveals that the two prominent peaks in the graph correspond to the emission of biogas from sewage wells located at the intersection of Yuquan Road and Lianshi Road and at the intersection of Nongda South Road and Yuanmingyuan West Road. According to Table 1, there is no significant seasonal variation in CH_4 concentration on the road during the morning rush hour. The average concentrations measured during the same time period over five days ranged from 2.08 ppm to 2.17 ppm. The average concentration for three days in April was 2144.95 ppb, which is 11.67% higher than the NOAA-published global average CH_4 concentration of 1920.74 ppb for March. This indicates that the CH_4 concentration on the experimental road is closer to the global average compared to the CO_2 concentration, as CH_4 is not influenced by exhaust emissions from fuel-powered vehicles.

The variations in CO_2 and CH_4 concentrations measured during three time periods at night along the experimental route from north to south are shown in Figures 11 and 12, respectively. The statistical analysis data are presented in Table 2. From Figure 11, it can be observed that, similar to the morning rush hour, the CO_2 concentration on the road at night is primarily related to traffic congestion. The congested sections on this measurement route at night are relatively consistent. The concentration trends observed during different time periods exhibit good consistency. The areas with higher concentrations in the graph correspond to traffic signal intersections such as the intersection of Youyi Road and Dengzhuang South Road, the northern area of the intersection of Yuanmingyuan West Road and Nongda South Road, and the area near the Linglong Road overpass on the West Fourth Ring Road. The latter two locations are known for frequent instances of traffic congestion on this road. According to Table 2, there is no significant seasonal variation in CO_2 concentration on the road at night. The average concentrations measured over five days ranged from 504 ppm to 535 ppm. The average concentration for three days in April was 514.80 ppm, which is

34.82 ppm lower than during the morning rush hour. This difference can be attributed to lighter traffic congestion on the road at night compared to the morning rush hour.

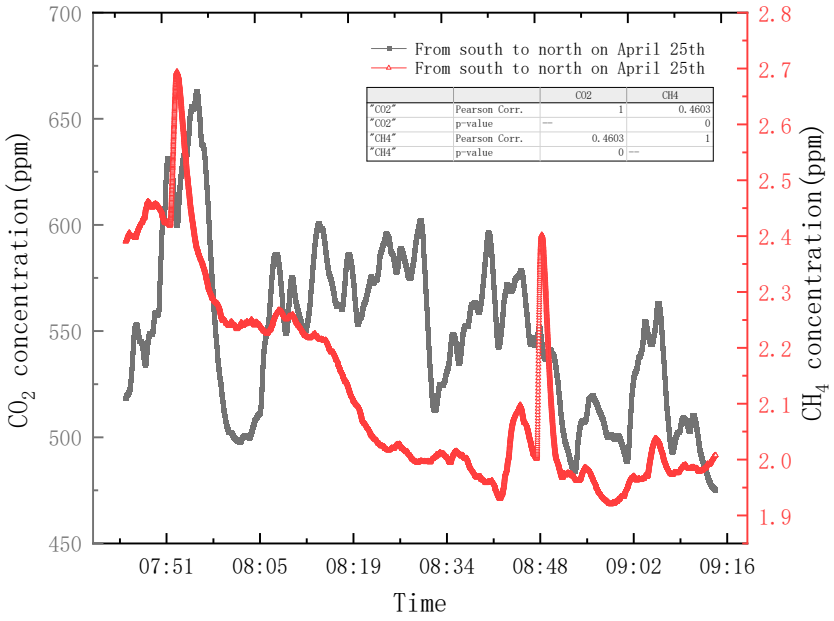

Figure 10. Correlation analysis of CO_2 concentration and CH_4 concentration measured from south to north on experimental road sections during morning rush hour.

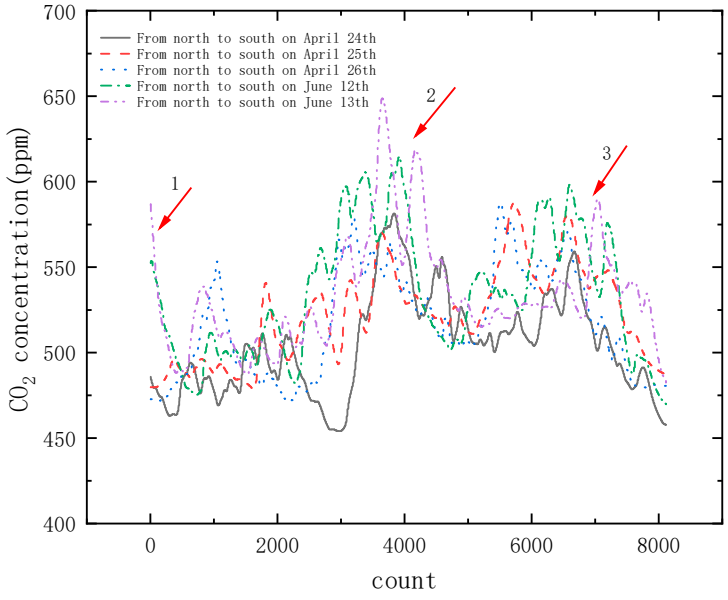

Figure 11. The CO_2 concentration from north to south on the experimental road section was measured during three time periods at night.

Figure 12 presents the correlation analysis between CO_2 and CH_4 concentrations measured during the night along the experimental route from north to south. The correlation between CO_2 and CH_4 concentrations is only 0.11, indicating almost no correlation between the two. From Figure 13, it can be observed that, similar to the morning rush hour, the CH_4 concentration on the road at night is not significantly related to traffic congestion but exhibits a clear increasing trend. This pattern reflects the diurnal variation in CH_4 concentration, where CH_4 levels tend to rise after sunset. The CH_4 concentrations measured at night in June are significantly lower than those measured in April. Similarly, the two prominent peaks in the graph correspond to the emission of biogas from sewage wells

located at the intersection of Nongda South Road and Yuanmingyuan West Road and at the intersection of Yuquan Road and Lianshi Road. According to Table 2, there is some seasonal variation in CH_4 concentration on the road at night. The CH_4 concentrations measured during the same time period in June are consistently lower than those in April. The average concentrations measured over five nights ranged from 1.95 ppm to 2.32 ppm. The average concentration for three nights in April was 2290.42 ppb, which is 145.47 ppb higher than during the morning rush hour. However, the average concentration measured over two nights in June was 171.16 ppb lower than during the morning rush hour. This indicates that the variation in CH_4 concentration during the night and morning rush hour does not follow a specific pattern.

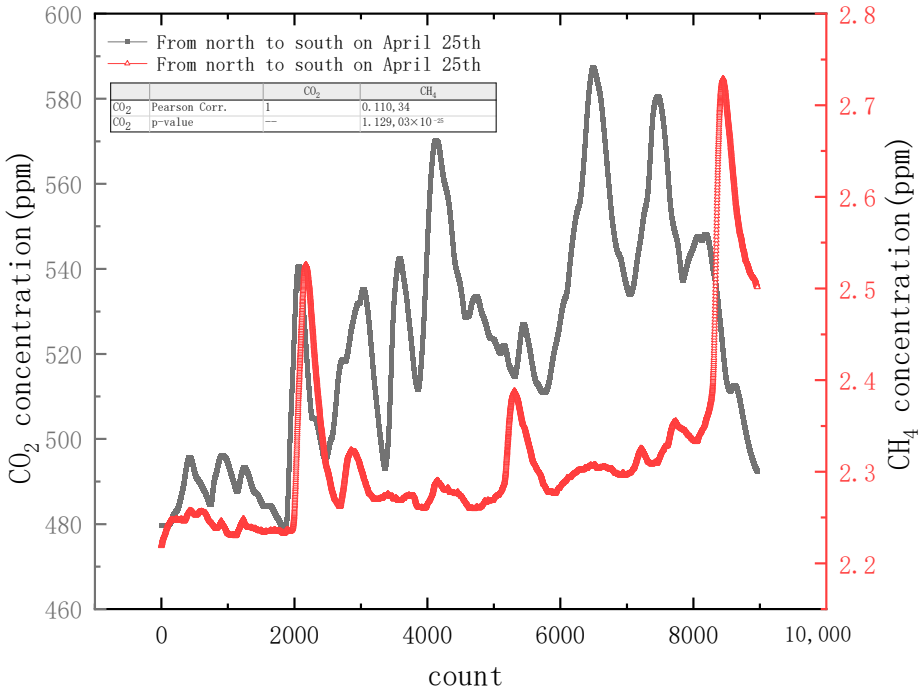

Figure 12. Correlation analysis of CO_2 concentration and CH_4 concentration from north to south on experimental road section at night.

Table 2. Statistical analysis of CO_2 and CH_4 concentrations measured at night.

Gas	Date	Period	Mean Value (ppm)	Standard Deviation (ppm)	Minimum Value (ppm)	Median (ppm)	Maximum Value (ppm)
CO_2	24 April 2023	19:00–20:01	504.6	29.9	454.1	504.5	581.4
	25 April 2023	20:38–21:19	522.3	27.4	478.5	521.9	587.3
	26 April 2023	21:20–22:14	517.6	31.6	471.6	514.3	587.4
	12 June 2023	20:03–20:58	534.5	37.4	469.8	532.8	614.8
	13 June 2023	19:13–20:01	533.8	32.4	482.5	527.2	648.8
CH_4	24 April 2023	19:00–20:01	2.237	0.022	2.204	2.232	2.356
	25 April 2023	20:38–21:19	2.314	0.095	2.219	2.287	2.729
	26 April 2023	21:20–22:14	2.320	0.035	2.221	2.314	2.520
	12 June 2023	20:03–20:58	1.951	0.046	1.870	1.956	2.073
	13 June 2023	19:13–20:01	2.040	0.066	1.877	2.031	2.223

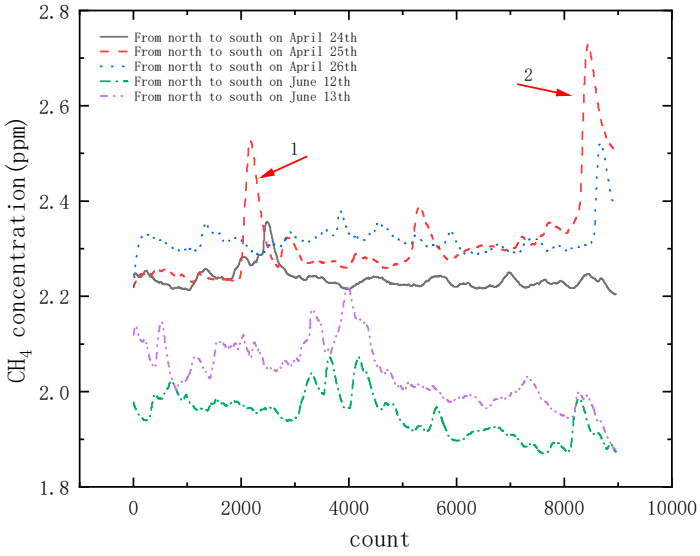

Figure 13. The CH_4 concentrations measured during three time periods at night along the experimental route from south to north.

5. Conclusions

A vehicle-mounted system capable of simultaneously detecting CO_2 and CH_4 was developed. By combining the tunable diode laser absorption spectroscopy (TDLAS) and derivative absorption spectroscopy techniques, the system achieved superior performance with a response time of 0.38 s and detection sensitivities of 5 ppb for CH_4 and 0.2 ppm for CO_2. Using this self-developed system, monitoring campaigns were conducted on the same road running north–south in Beijing during April and June 2023. The spatiotemporal variations of CO_2 and CH_4 concentrations on the road were obtained, verifying the feasibility of using the self-developed system for vehicle-mounted detection of greenhouse gas concentrations on urban ground roads. Additionally, the system implemented low-power, long-term, stable operation through modules such as the laser temperature control module, current driving module, and sawtooth signal generation module. By adding or replacing different lasers, it can be used for measurements of different gas component concentrations, providing a reference for the compact design of portable mobile platform TDLAS measurements. These research results also provide data for analyzing the spatial patterns of regional carbon sources and sinks. The next plan is to add temperature and pressure sensors to the absorption cell, implement temperature and pressure control, and further improve the system's detection accuracy.

Author Contributions: Conceptualization, J.C.; data curation, J.C. and S.C.; formal analysis, P.C. and H.W.; funding acquisition, C.Z. and L.J.; investigation, L.J., H.Z., L.C. and Y.Q.; methodology, J.C.; project administration, M.Z.; validation, J.C., C.Z., X.Y. and G.T.; writing—original draft, J.C.; writing—review and editing, J.C. and P.C. All authors have read and agreed to the published version of the manuscript.

Funding: This research was funded by the project for multidimensional information modeling technology for typical scenarios in underground spaces, grant number E1MZ060106, The Natural Science Foundation of Zhejiang Province Public Welfare Project, grant number LGF22C160002, and The Key Deployment Project of Aerospace Information Research Institute of Chinese Academy of Sciences, grant number E0Z206020F.

Institutional Review Board Statement: Not applicable.

Informed Consent Statement: Not applicable.

Data Availability Statement: The data presented in this study are available from corresponding authors.

Conflicts of Interest: The authors declare no conflict of interest.

References

1. Hansen, J.; Ruedy, R.; Sato, M.; Lo, K. Global surface temperature change. *Rev. Geophys.* **2010**, *48*. [CrossRef]
2. Solomon, S. IPCC (2007): Climate change the physical science basis. In *Proceedings of the AGU Fall Meeting Abstracts*; Cambridge University Press: Cambridge, UK, 2007.
3. Wunch, D.; Toon, G.C.; Blavier, J.-F.L.; Washenfelder, R.A.; Notholt, J.; Connor, B.J.; Griffith, D.W.; Sherlock, V.; Wennberg, P.O. The total carbon column observing network. *Philos. Trans. R. Soc. A Math. Phys. Eng. Sci.* **2011**, *369*, 2087–2112. [CrossRef] [PubMed]
4. Global Monitoring Laboratory. Available online: https://gml.noaa.gov/ccgg/trends/global.html (accessed on 4 April 2023).
5. Wei, C.; Wang, M.; Fu, Q.; Dai, C.; Huang, R.; Bao, Q. Temporal characteristics of greenhouse gases (CO_2 and CH_4) in the megacity Shanghai, China: Association with air pollutants and meteorological conditions. *Atmos. Res.* **2020**, *235*, 104759. [CrossRef]
6. Reum, F.; Gerbig, C.; Lavric, J.V.; Rella, C.W.; Göckede, M. Correcting atmospheric CO_2 and CH_4 mole fractions obtained with Picarro analyzers for sensitivity of cavity pressure to water vapor. *Atmos. Meas. Tech.* **2019**, *12*, 1013–1027. [CrossRef]
7. Cheng, H.; Wang, M.; Wen, Y.; Wang, G. Background concentration of atmospheric CO_2, CH_4 and N_2O at Mt.Waliguan and Xinglong in China. *J. Appl. Meteorol. Sci.* **2003**, *14*, 402–409.
8. Macatangay, R.; Warneke, T.; Gerbig, C.; Körner, S.; Ahmadov, R.; Heimann, M.; Notholt, J. A framework for comparing remotely sensed and in-situ CO_2 concentrations. *Atmos. Chem. Phys.* **2008**, *8*, 2555–2568. [CrossRef]
9. Hartmann, J.-M.; Tran, H.; Toon, G. Influence of line mixing on the retrievals of atmospheric CO_2 from spectra in the 1.6 and 2.1 μm regions. *Atmos. Chem. Phys.* **2009**, *9*, 7303–7312. [CrossRef]
10. Zhang, X.; Hu, N.; Xiao, W.; Liu, S.; Zhang, X.; Zhang, S. Analysis on atmospheric carbon dioxide and methane concentrations by using mobile vehicle-mounted observations in urban routes. *Environ. Sci. Technol.* **2020**, *43*, 83–89.
11. Zhang, M.; He, D.; Gu, T.; Sun, T.; Lin, X.; Huang, X.; He, L. Characteristics of greenhouse gas emissions from road traffic sources in Shenzhen. *China Environ. Sci.* **2022**, *42*, 1518–1525.
12. Li, R.N.; Wang, J.; Liu, Y.Z.; Chen, L.L.; Zhang, M.; Cao, C.; Qi, B.; Hu, N.; Xiao, W. Spatial representativeness of urban observation sites and hotspot identification based on CO_2/CH_4 vehicle-carried mobile observations. *China Environ. Sci.* **2023**, *43*, 2106–2118.
13. Zhao, B.; Yu, L.; Wang, C.; Shuai, C.; Zhu, J.; Qu, S.; Taiebat, M.; Xu, M. Urban air pollution mapping using fleet vehicles as mobile monitors and machine learning. *Environ. Sci. Technol.* **2021**, *55*, 5579–5588. [CrossRef]
14. Siozos, P.; Psyllakis, G.; Velegrakis, M. Remote Operation of an Open-Path, Laser-Based Instrument for Atmospheric CO_2 and CH_4 Monitoring. *Photonics* **2023**, *10*, 386. [CrossRef]
15. Liu, Y.; Liu, Y.; Zhao, Y.; Wu, W.; Yao, L.; Liu, Z. Development of the carbon dioxide laser detection system for grain storage based on TDLAS. *Trans. Chin. Soc. Agric. Eng. (Trans. CSAE)* **2022**, *38*, 250–256. [CrossRef]
16. Du, B.-L.; Li, M.; Guo, J.J. The Experimental Research on In-Situ Detection for Dissolved CO, in Seawater Based on Tunable Diode Laser Absorption Spectroscopy. *Spectrosc. Spectr. Anal.* **2022**, *42*, 1264–1269.
17. Wang, B.; Dai, T.; Cheng, L.; Zhang, R.; Yu, Y.; Lian, H. Design of methane and carbon dioxide detection system based on VCSEL laser. *Laser J.* **2022**, *43*, 15–19. [CrossRef]
18. Zhang, L. *Investigations on Measurement of Low Concentration Andmulti-Component Gas and Reconstruction of 2D Temperature and Concentration Distribution Using Laser Absorption Spectroscopy*; Zhejiang University: Hangzhou, China, 2017.
19. Xu, Z.; Liu, W.; Kan, R.; Zhang, Y.; Liu, J.; Zhang, S.; Shu, X.; Geng, H.; He, Y.; Tang, Y. Study on the Arithmetic of Absorbance Inversion Based on Tunable Diode-Laser Absorption Spectroscopy. *Spectrosc. Spectr. Anal.* **2010**, *30*, 2201.
20. Chen, J.; Liu, J.; He, Y.; Xu, Z.; Li, H.; Yao, L.; Yuan, S.; Ruan, J.; He, J.; Kan, R. Temperature Measurement of CO_2 by Use of a Distributed-Feedback Diode Laser Sensor Near 2.0 μm. *Chin. J. Lasers* **2012**, *39*, 1108004. [CrossRef]
21. Fan, F.; Song, Z. Measurement of CO_2 Concentration with Tunable Diode Laser Absorption Spectroscopy near 2 μm. *Chin. J. Lasers* **2012**, *39*, 0215002.
22. He, J.; Kan, R.; Xu, Z.; Duan, L.; Wang, X. Derivative Spectrum and Concentration Inversion Algorithm of Tunable Diode Laser Absorption Spectroscopy Oxygen Measurement. *Acta Opt. Sin.* **2014**, *34*, 0430003.
23. Chen, B.; He, G.; Zuo, W.; Wen, J. Long Path Gas Chamber with Stable Packaging Structure. Patent NO. CN201610036719. X, 9 June 2023.
24. János, I.; Tamás, L.; Allan, M.U. *Compendium of Analytical Nomenclature: Definitive Rules 1997*; Blackwell Science: Oxford, UK, 1998.